Materials Today Energy 32 (2023) 101231

Contents lists available at ScienceDirect

Materials Today Energy

journal homepage: www.journals.elsevier.com/materials-today-energy/

Efficient ethanol electro-reforming on bimetallic anodes supported on adenine-based noble carbons: hydrogen production and value-added chemicals

Alberto Rodríguez-Gómez [a], Enrico Lepre [b], Fernando Dorado [a], Luz Sanchez-Silva [a], Nieves Lopez-Salas [b], Ana Raquel de la Osa [a,*]

[a] Faculty of Chemical Sciences and Technology, University of Castilla-La Mancha, Enrique Costa Novella Building. Avda. Camilo José Cela, 12, Ciudad Real, 13071, Spain
[b] Colloid Chemistry Department, Max Planck Institute of Colloids and Interfaces, Am Mühlenberg 1, Potsdam, 14476, Germany

ARTICLE INFO

Article history:
Received 25 October 2022
Received in revised form
14 December 2022
Accepted 15 December 2022
Available online 22 December 2022

Keywords:
Adenine-based noble carbon
Ethanol electrooxidation
PEM cell
Green Hydrogen
Chemicals production

ABSTRACT

Herein, adenine-derived noble carbons are used as anodic supports for PtRu nanoparticles for the ethanol oxidation reaction (EOR). Three noble carbons were synthesized using salt melts as templates and denoted as ANZ, ALZ and ALK depending on the precursor ($LiCl/ZnCl_2$, $NaCl/ZnCl_2$ and LiCl/KCl). Their large nitrogen content and pore volume (ANZ > ALZ > ALK) facilitate the formation of small PtRu nanoparticles (2–3 nm), while variations in the C/N ratio and surface area deeply affected the alloy formation (0–58%). In a half-cell configuration, PtRu/ANZ exhibited the highest activity (443 mA/mg_{PtRu}), followed by PtRu/ALZ and PtRu/ALK, due its higher dispersion degree and lower alloying percentage. More interestingly, PtRu/ANZ and PtRu/ALZ presented 2.4 and 1.6 larger mass activity than commercial PtRu/C. Regarding the ethanol electrolysis, the best materials were scaled up to a proton exchange membrane cell. Acetaldehyde was the major compound followed by acetic acid and ethyl acetate (anode), while hydrogen was produced with 100% faradaic efficiency (cathode). PtRu/ANZ provided the best electrochemical performance, shifting the acetic acid production to a lower potential (0.6 V), requiring lower energy ($\sim$ 35 kWh/kg_{H_2} at 1 A) than commercial water electrolyzers. These promising results set a precedent for high nitrogen containing supports for EOR electrocatalysts.

1. Introduction

The current energy crisis mainly arises from the excessive use of fossil fuels as the major way to supply the global energy demand. To continue with this high level of consumption, society requires large volumes of fuels especially in transport and energy sectors, where carbon dioxide emissions are considerably high [1]. From the perspective of sustainability and circular economy, hydrogen has recently been postulated as a promising substitute to fossil fuels. Among all hydrogen production processes, ethanol electrolysis (also called electrochemical reforming or electroreforming) is being considered as an attractive option since it provides further energy savings compared to water electrolysis (>50%) [2]. Also, ethanol can be obtained through physicochemical and biological transformations of vegetable raw materials such as beets or sugar cane, among others [3]. In an electrolyzer, ethanol oxidation reaction (EOR) takes place in the anodic chamber, generating electro-oxidized organic products, protons and electrons whereas hydrogen evolution reaction (HER) occurs in the cathodic compartment. In the case of a proton exchange membrane (PEM) cell, protons are transported from the anode to the cathode (acid media) through a solid electrolyte (Nafion membrane) to produce hydrogen gas. Although most literature concerning ethanol electroreforming focuses only on the hydrogen production, the previous configuration allows the co-production of value-added organic compounds in the anodic effluent such as acetaldehyde, acetic acid or ethyl acetate. In this sense, electrochemical reforming can be used to exploit the ethanol partial oxidation to valuable intermediates of industrial interest apart from hydrogen [4–6]. Regarding anodic electrocatalysts, the high current performance of the PEM electrolyzers entails the use of expensive Pt-based

* Corresponding author.
E-mail address: AnaRaquel.Osa@uclm.es (A.R. de la Osa).

https://doi.org/10.1016/j.mtener.2022.101231

electrodes, being PtRu/C and PtSn/C among the most efficient anodes due to the promotion of the bifunctional mechanism [7,8].

One of the possible strategies to reduce the catalyst cost is the optimization of the support, which is not a mere substrate, but it can modify the morphology of the nanoparticles and acts as a promoter of the electrochemical reaction. Among all types of electrocatalytic supports, carbon materials outstand because of their versatility (i.e. many different physico-chemical properties such as their composition, porous network, or conductivity can be readily modified) [9–11]. For instance, the use of multiwalled carbon nanotubes (MWCNTs), carbon nanofibers (CNFs) or graphene as a catalytic support for metal nanoparticles dispersion enhanced the EOR activity [12–14]. Other studies have shown that doping carbonaceous materials with heteroatoms (i.e. oxygen, nitrogen, sulfur, phosphorous or boron) is an effective way to tune their intrinsic properties. The substitute heteroatoms can provide more initial nucleation sites for the formation of noble metal nanoparticles and also enhance the interaction between nanoparticles and support increasing the chemical binding energy [15]. Thus, nitrogen-doped CNTs have proved to increase the electrocatalytic activity of PtRu nanoparticles toward methanol and ethanol oxidation [13,16]. Heteroatom doping can be achieved via post-treatment of the materials with the corresponding heteroatom precursor or, by choosing a carbonaceous precursor containing the desired heteroatom. In this context, carbonization of nucleobases is of great interest due to (i) their inherent large nitrogen content, (ii) the potential stability towards oxidation induced by the carbonization of very stable molecules and, (iii) because of their pre-coded basic nitrogen functionalities. The resulting carbonaceous materials are known as 'noble carbons' (NC) and their pore network can be extensively tuned using different salt mixes as structure-directing agents during the carbonization process [17]. A recent work from our group reports that the particle size and alloy composition of a PtRu metallic active phase strongly depends on the composition and pore architecture of highly N-doped porous noble carbons derived from cytosine [18]. Such noble carbon supports provided a better nanoparticle dispersion due to their intrinsic large nitrogen content and increased stability at high potentials due to its high resistance upon oxidation (compare to conventional carbon black). Despite all these advantages, the overall electrocatalytic activity of these materials was similar to those obtained for the carbonaceous materials mentioned above, being a first approach in the NC use for the EOR development. Therefore, in this work, we propose the use of adenine instead of cytosine as carbon precursor to synthesize carbon supports for PtRu EOR anodes. Compared to cytosine, adenine holds a smaller initial C/N ratio (i.e. 1) and its xanthine chemical structure comprising imidazolium rings confers to the molecule larger stability. That makes adenine a promising carbonaceous precursor [19,20]. For instance, adenine was already used as an additive enhancing the performance of ionic liquid derived carbon materials for their use as electrocatalysts for the oxygen reduction reaction (ORR) [21]. Moreover, Pampel et al. also used adenine as carbonaceous precursor for the preparation of electrodes for the same application, finding out that hierarchical carbon materials could be prepared by using $NaCl/ZnCl_2$ molten salts [22].

Herein, we report the influence of different adenine-based noble carbon (ANCs) supports on the electrochemical oxidation of ethanol. To that purpose, carbonaceous materials were prepared through various template agents ($LiCl/ZnCl_2$, $NaCl/ZnCl_2$ and LiCl/KCl) and subsequently used for the synthesis of anodic PtRu/ANCs electrocatalysts. The variation of the porous architecture (depending on the salt mix) and electrocatalyst morphology were analyzed through different characterization techniques before and after the nanoparticles decoration. The electrochemical performance toward the EOR was preliminary explored in a half-cell configuration. Finally, the best materials were scaled-up to a PEM cell configuration to evaluate their technical viability for clean hydrogen and organic compounds production.

2. Experimental section

2.1. Materials and chemicals

All the materials were used as received without further purification. Adenine (99%) and zinc chloride (98%) were purchased from Merck. Potassium chloride (99%), lithium chloride (98%) and sodium chloride (98%) were purchased from Fischer chem. 1 M hydrochloric acid was purchased from Roth. Hexachloroplatinic acid hexahydrate ($H_2PtCl_6 \cdot 6H_2O$) and ruthenium chloride ($RuCl_3$) were purchased from Alfa Aesar. Ethylene glycol (99%), ethanol (96%), 2-propanol (99.9%), $HClO_4$ (60%) and Nafion aqueous solution (5 wt %) were purchased from Sigma Aldrich. NaOH (pellets) was purchased from Panreac. Deionized water (18.2 MΩ cm) used in all the experiments was provided by a Milli-Q Labo apparatus. The commercial cathode, i.e. Pt/C catalyst with 20 wt% of a total metal loading as well as the polymeric membrane (Nafion 117) were purchased from Sigma Aldrich.

2.2. Synthesis of adenine-based noble carbon (ANCs) supports

Typically, 2 g of adenine with 20 g of LiCl and 20 g of $ZnCl_2$ were mixed in an Agatha mortar. The mixture was heated at 1 °C/min in N_2 atmosphere to 800 °C. That temperature was kept for 2 h. After spontaneous cooling down the sample was washed twice in 500 mL of 1 M HCl aqueous solution at room temperature and left overnight. After that, the sample was washed two times with 150 mL HCl 1 M at 50 °C. Samples were then filtered and dried at 70 °C for 5 h (1 atm) and 150 °C overnight (5 mbar). The dried carbon powder was obtained with a 30% yield. The sample was named as ALZ where 'A' stands for adenine, 'L' stands for lithium chloride and 'Z' stands for zinc chloride. Samples ANZ and ALK were prepared using the same procedure and 'N' and 'K' stand for NaCl and KCl, respectively. For example, the preparation of ANZ comprises 2 g of adenine (as precursor), 20 g of $ZnCl_2$ and 20 g of NaCl (templating agents). In the same way, ALK samples were synthesized using 2 g of adenine, 24 g of LiCl and 16 g of KCl. After the heat treatment, ANZ and ALK were washed and dried as explained for ALZ.

2.3. Synthesis of PtRu/ANCs electrocatalysts

PtRu nanoparticles supported on each as-prepared carbonaceous material were synthesized using the modified polyol method. In a standard procedure, precursors salts ($H_2PtCl_6 \cdot 6H_2O$ and $RuCl_3$) were dissolved in 50 mL of ethylene glycol. Proper amounts of NaOH were added to the initial solution in order to control the pH during the synthesis process. The mixture was stirred for 1 h at room temperature, then the temperature was increased to 190 °C for 2 h leading to the *in-situ* co-reduction of the mixed precursors salts. After the completion of the reduction process, an appropriate amount of each ANCs support (i.e. ANZ, ALZ or ALK) was subsequently added to result in 60 wt% of metal loading with a 2:1 mass ratio between Pt and Ru. The colloidal mixture was cooled down and stirred for 48 h. Particles were then filtered, washed with an excess of deionized water (18.2 MΩ cm), and dried at 80 °C overnight.

2.4. Physicochemical characterization

Powder X-ray diffraction patterns of the carbon supports were recorded in a Bruker D8 Advance instrument using a Cu-Kα radiation source (λ = 0.154 nm) and NaI scintillation counter-Scinti-Detector. The patterns were recorded in a 2θ range between 5 and 70° using 0.05° steps and 2 s. Thermogravimetric analysis (TGA) was measured in a Thermo Microbalance TG 209 F1 Libra (Netzsch, Selb, Germany). Traces were recorded using Pt crucibles and with a 20 cm^3/min flow of nitrogen or synthetic air as carrier gas. The heating rate was 10 K/min and the mass of sample analyzed 0.01 g. The X-ray diffraction patterns after the nanoparticles deposition were recorded on a Philips X'Pert MPD instrument using nickel-filtered Cu K_α radiation ($\lambda = 1.54056$ Å). The spectra were recorded from $2\theta = 5{-}90°$ with a 0.02° step size using an acquisition time of 2 s per step. The phases were identified by comparing them with JCPDS (Joint Committee on Powder Diffraction Standards) files. The average crystal size was determined through the Debye-Scherrer equation.

Inductively coupled plasma optical emission spectrometry (ICP-OES) was carried out using a PerkinElmer ICP-OES Optima 8000. Each element was calibrated using four calibration standard solutions to obtain a calibration curve. 0.01 g of each measured sample were dissolved using a 1:2 mixture of HNO_3 and HCl (500 μL) of and kept at room temperature for 12 h in the solution and then at 96 °C for 1 h. After digestion, the samples were diluted up to 10 mL using ultrapure water. Samples were filtrated before measurement. The data given are the average of values obtained after triplicated analyses of each sample. Scanning electron microscopy (SEM) micrographs were recorded in a LEO 15550-Gemini instrument from Zeiss after sputtering samples with ca. 10 nm layer of an 80% gold/20% platinum mixture. Energy-dispersive X-ray (EDX) spectra were recorded through a coupled EDX analyzer (Oxford instruments). High-Resolution Transmission Electron Microscopy (HRTEM) and High Angular Annular Dark Field Scanning Transmission Electron Microscopy (HAADF-STEM) coupled with Energy Dispersive X-ray Spectroscopy (EDX) were obtained using a FEI Talos F200X equipment operating at an accelerating voltage of 200 kV. Each sample was drop casted in copper TEM grids from an ethanol dispersion.

A Quantachrome Quadrasorb SI instrument was used to run N_2 adsorption/desorption isotherms at 77 K and CO_2 adsorption isotherms at 273 K. Samples were submitted to a degassing procedure in a 3P Instruments Masterprep degassing machine prior to each analysis. The degassing was carried out at 150 °C and 0.5 Torr for 20 h. The Brunauer-Emmett-Teller (BET) method was used to calculate the specific surface area of the samples using data under $P/P_0 < 0.2$. The total pore volume (V_T) of the samples was obtained from the amount of N_2 (or CO_2) adsorbed at $P/P_0 = 0.995$. Quenched Solid Density Functional Theory (QSDFT) kernel of carbon materials comprising slit/cylindrical pores was selected to calculate the pore size distribution from the adsorption branch of N_2 isotherms at 77 K.

Temperature-programmed reduction (TPR) experiments were conducted using a Micromeretics AutoChem 2950 HP unit equipped with a TCD detection system. Samples (ca. 0.08 g) were deposited into a U-shaped tube reactor and ramped from room temperature to 900 °C (10 °C/min). To that purpose a reducing gas mixture of 5% H_2/Ar (60 cm^3/min) was used.

X-ray photoelectron spectroscopy (XPS) measurements were performed using a ThermoScientific Escalab 250 Xi instrument. Analyses were run using a micro-focused, monochromatic Al Kα X-ray source (1,486.68 eV). The spot size for the analysis was 400 μm.

2.5. Electrochemical characterization in a three electrodes cell

Electrochemical data were recorded using a potentiostat/galvanostat instrument Autolab PGSTAT128 N (Eco Chemie, Netherlands) operated by NOVA 2.1 software. The electrochemical measurements were conducted at room temperature in a conventional three-electrode glass cell which consists of a catalyst coated glassy carbon (GC) rotating disk electrode (GC-RDE, Metrohm) of 0.19 cm^2 surface area as the working electrode, a platinum foil as the counter electrode and Ag/AgCl (saturated in 3 M KCl, Metrohm) as the reference electrode. Prior to use, the surface of the GC was polished with an alumina suspension and rinsed with distilled water. Also, all the potential values were referred to the reversible hydrogen electrode (RHE) according to the Nernst equation. The catalyst powder solutions or 'inks' were formed by dissolving 2 mg of the noble carbon-supported electrocatalysts in 750 μL of isopropanol, 250 μL of deionized water and 8 μL of Nafion solution. After sonicating the ink for 30 min, an aliquot of 10 μL of the solution was deposited onto the GC surface reaching a total metal loading of 0.063 mg/cm^2 and then dried at room temperature for 2 h. In all experiments, the electrolyte was deaerated by bubbling N_2 for 20 min and then the inert atmosphere was maintained over the solution during the test performance. Also, the working electrode was rotated at 100 rpm to achieve a homogenous and uniform catalyst film.

The electrochemical active surface area (ECSA) was evaluated by cyclic voltammetry essays (CVs) in absence of ethanol (0.25 M $HClO_4$ electrolyte) for a potential interval from −0.038 to 1.4 V vs. RHE with a sweep rate of 50 mV/s. To evaluate the electrocatalyst degradation, an accelerated degradation test (ADT) was conducted by performing 500 cycles at the same conditions mentioned above. The degradation degree was estimated by the ECSA losses between the first and last cycle. The electrochemical activity toward the EOR was explored in 4 M EtOH + 0.5 M $HClO_4$ electrolyte by applying a potential interval from 0 to 1.2 V vs. RHE at a scan rate of 10 mV/s. The anti-poison ability of PtRu/ANCs was performed through CO-Stripping measurements. Prior to the test, CO was introduced for 20 min at 0.2 V vs. RHE to ensure the adsorption on the catalyst surface. After CO saturation, the electrolyte was degassed using a N_2 stream to eliminate the excess of CO. CV profiles were then obtained from a potential range of 0−1.2 V vs. RHE at 20 mV/s of scan rate. Finally, to study the stability, a long-term chronoamperometry test was carried out at a fixed potential of 0.7 V vs. RHE for 10 h.

2.6. Proton exchange membrane (PEM) electrolysis cell

Electrochemical reforming experiments were performed in a PEM electrolysis cell SQUAEREPARK 5 (Pragma industries, France) with an active surface area of 5 cm^2. All cell components are described in detail elsewhere [5]. Synthesized bimetallic PtRu/ANCs were used as anode while commercial Pt/C was adopted as the cathode. Catalyst inks were prepared by mixing appropriated amounts of the catalyst powders (12.5 mg) with Nafion solution and 2-propanol with a binder/catalyst mass ratio of 3.64. For the MEA preparation, inks were directly sprayed on both sides of the Nafion 117 membrane at 80 °C without the requirement of a high temperature/pressure assembly step. Total metal loading was 1.5 mg/cm^2 and 0.5 mg/cm^2 for anode and cathode, respectively. The contact between the catalytic layer and the gas diffusion layer (carbon paper TGP-H90, Fuel Cells Earth) was accomplished by the simple sandwich of the different cell components (Monopolar plates, Teflon gaskets, membrane, etc.). This novel cell configuration proved to be more advantageous in decreasing the diffusional limitations [23]. The anodic compartment of the cell was then fed

with an aqueous fuel solution (4 M of ethanol solution) at a flow rate of 1.15 mL/min while the cathodic chamber was supplied with deionized water at 1.65 mL/min. To that aim, a multichannel peristaltic pump (5001, Heidolph) was used for both anodic and cathodic streams operating in continuous mode (without recycling). The feeding solutions were preheated at a temperature close to that of the electrochemical cell (80 °C) and a cooling condensation column was installed in the anodic reservoir (−5 °C) to avoid ethanol evaporation.

Electrochemical measurements were carried out using a potentiostat/galvanostat VERTEX 5 V (Ivium Technology) controlled by a research electrochemistry software. Linear sweep voltammetry (LSV) tests were carried out with a gradual polarization from 0 to 1.4 V at a scan rate of 20 mV/s. Chronopotentiometry essays were conducted at different fixed current levels (0.2−1.4 A, i.e. 40−280 mA/cm^2) maintaining each level for 900 s. The product distribution was evaluated along with the total ethanol conversion for each applied current step. Analyses of the liquid products were carried out using a high-performance gas chromatograph GC (Agilent Technologies 8220 A), equipped with an FID detector and a capillary column (Agilent DB-WAS UI, 30 m × 0.2 mm × 0.25 μm) using helium as a carrier gas. Although the liquid products from the alcohol electrolysis are generated in the anodic chamber, the cathodic effluent was also analyzed to avoid inaccuracies in the product distribution due to the crossover membrane effect. To that aim, an aliquot of 2 mL was taken from both output cell streams and analyzed offline in the GC. The rate of hydrogen production during the electrochemical reforming experiments was also followed by gas-volume measurements and crosschecked via Faraday's Law equation, based on the cell current values.

3. Results and discussion

3.1. Physicochemical characterization

3.1.1. Adenine-based noble carbon (ANCs) supports

The use of inorganic salt mixes as solvents and structure-directing agents to prepare carbonaceous materials is a well-established strategy [24]. In general terms, the melting of the inorganic salt mix should occur before the decomposition or sublimation of the selected carbon precursor. When this occurs, the melted inorganic salt mix is able to dissolve the carbon precursor, which then condenses and precipitates out of the melted ionic mix forming a structured carbon. Herein, we study the effect of using different inorganic salt mixes (i.e. 1:1 w/w NaCl:$ZnCl_2$, 1:1 w/w LiCl:$ZnCl_2$ and 3:2 w/w KCl:LiCl) as high temperature solvents and structure-directing agents to prepare carbonaceous materials using adenine as carbonaceous precursor. The ratio and composition of the inorganic mixes affect the temperature at which they melt. The ratio of the inorganic mixes was chosen so the melting temperatures would not exceed 400 °C (i.e. the expected sublimation temperature of adenine). The melting temperatures were 325, 330 and 352 °C for 1:1 w/w NaCl:$ZnCl_2$, 1:1 w/w LiCl:$ZnCl_2$ and 3:2 w/w KCl:LiCl. The 3:2 w/w KCl:LiCl ratio yielded the lower melting point for this inorganic mix. Adenine was blended with the different mixes in a 1:20 w/w ratio and submitted to heat treatment at 800 °C for 2 h (1 K/min). The different samples will be named hereafter as ALZ, ANZ and ALK, where LZ, NZ and LK stands for 1:1 w/w LiCl:$ZnCl_2$, 1:1 w/w NaCl:$ZnCl_2$ and 3:2 w/w KCl:LiCl, respectively. As can be seen in Table 1, samples were obtained in large yields for the heat treatment of a not polymeric precursor, i.e. 30, 40 and 25% for ANZ, ALZ and ALK, respectively. This is an interesting result considering that adenine thermogravimetric analysis indicates that it tends to sublimate upon thermal treatment at ca. 200 °C (Figure S1a). Table 1 indicates that the salt mixes probably catalyze the formation of intermediate condensation products that prevent the sublimation of adenine and foster larger yields of carbonaceous product. This phenomenon has been also observed in the synthesis of carbonaceous materials using other small organic molecules [25].

Table 1
Summary of the physicochemical parameters obtained for the different carbonaceous supports by N_2 adsorption-desorption isotherms at 77 K and CO_2 adsorption-desorption isotherms at 273 K.

Sample	Yield (%)	C/N ratio	S_{BET} (m^2/g)[a]	V_{T,N_2} (cm^3/g)[b]	V_{mic,CO_2} (cm^3/g)[c]
ANZ	30	5.7	2292	1.945	0.276
ALZ	40	5.6	2334	2.500	0.211
ALK	25	2.1	389	0.955	0.117

[a] Specific surface area was calculated from nitrogen adsorption data ($P/P_0 < 0.2$) using the Brunauer-Emmett-Teller (BET) method.
[b] Total pore volume (V_T) was calculated from the amount of nitrogen adsorbed at $P/P_0 = 0.995$.
[c] Total micropore volume was calculated from the amount of carbon dioxide adsorbed at 730 Torr.

XRD patterns of the adenine-based carbonaceous materials prepared using $ZnCl_2$ showed an almost flat diffractogram indicating the lack of graphitic stacks and amorphous nature of the samples (Figure S1b). A striking difference is observed when comparing the diffractograms of ANZ and ALZ with ALK. Unlike the former, ALK shows a clear diffraction peak at 27° indicating the presence of graphitic stacks and points to a different condensation mechanism for the carbonization of adenine in the presence of LK.

Elemental analyses also revealed that the C/N ratio of the samples strongly depends on the used molten salt (Table 1 and Table S1). For instance, NZ and LZ mixes give rise to samples with a ca. 5.5 C/N ratio while LK salt mix sample has a C/N ratio of 2.1. ICP analyses of the samples indicate that, after washing with HCl, the carbonaceous supports only contain residual amounts of metals (Table S2). X-ray photoelectron spectroscopy (XPS) was performed in order to understand the chemical differences induced in the samples by the use of the different salt mixes. C1s deconvoluted XPS spectra of the three samples consist of three main peaks centered at 284.7 eV, 285.6 eV and 287.8 eV, typically ascribed to sp^2 C−C bonds, C−N bonds and adventitious C−O bonds (Fig. S2). The results indicate that the relative intensity of sp^2 C−C bonds with respect to C−N bonds increases from ALK to ANZ and to ALZ. The deconvolution of N1s peaks shows four components centered at 398.4 eV, 400.3 eV, 401.7 eV and a broad band at 404.4 eV which are ascribed to C−N=C nitrogen atoms, pyrrolic-N units, quaternary-N species and π-π* interactions (Fig. 1) [26]. The intensity of the peak ascribed to C−N=C motifs increases while the band ascribed to π-π* interactions decreases from sample ALZ to ANZ, and from ANZ to ALK. This indicates that LZ promotes the formation of a more conjugated carbon network than NZ or LK, as also seen in the deconvolution of the C1s. It is known that $ZnCl_2$ can have a catalytic effect on the dehydration reactions occurring upon carbonization [27,28]. However, the results of adenine derived carbons indicate that also LiCl and NaCl play a critical role in the formation of different N-functionalities. Moreover, the absence of $ZnCl_2$ promotes the formation of a nitrogen richer carbonaceous product comprising a larger amount of C−N=C nitrogen, a much lower amount of pyrrolic-N, and a much lower π−π* interaction band. Herein, it is important to highlight that, compared to noble carbons prepared from cytosine [18], all the samples derived from adenine show a larger proportion of pyridinic nitrogen which indicates they have more electron rich (basic) functionalities in the surface.

SEM micrographs of the samples in Fig. S3 evidence the different morphologies obtained by using the three molten salt mixes.

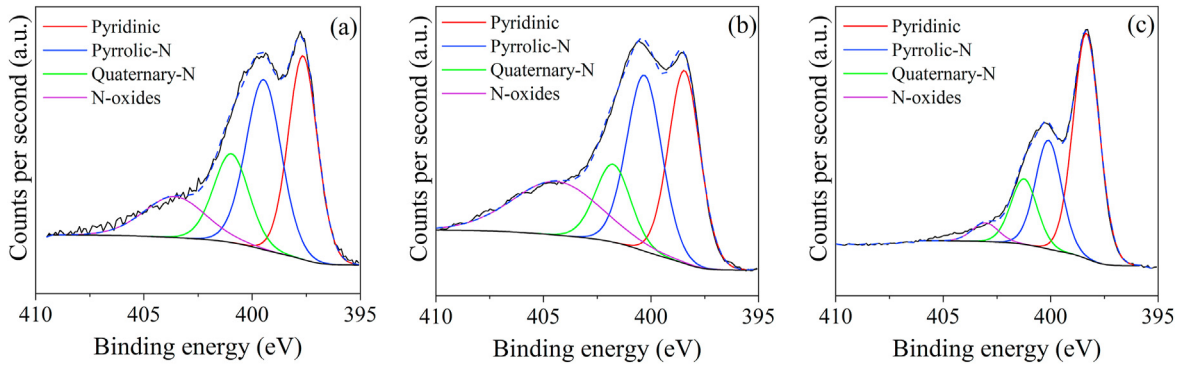

Fig. 1. N1s deconvoluted XPS spectra of a) ANZ, b) ALZ and c) ALK.

Samples prepared using $ZnCl_2$ based mixtures show a colloidal porous morphology with colloid sizes dramatically decreasing from ANZ to ALZ (i.e. from 50 nm to 15 nm, respectively). When LK is used as molten salt, the resulting material does not show a colloidal nature. This indicates that the precursor was not solubilized by the salt mix probably due to the higher melting point of LK compared to that of LZ or NZ (e.g. LK 352 °C, LZ 330 °C and NZ 325 °C). The higher melting point of LK allows the precursor to pre-condense before the inorganic mix melts thus, becoming insoluble in it and further condensing through a different mechanism, which corroborates the chemical differences observed by XPS.

N_2 adsorption-desorption isotherms at 77 K and CO_2 adsorption-desorption isotherms at 273 K were run to understand the porous architecture of the samples (Fig. 2). All samples show Type I and IV isotherm shapes indicating the presence of both micropores and mesopores in their pore networks. A summary of the parameters obtained from the isotherms is given in Table 1. ANZ and ALZ show much larger total pore volumes, micropore volumes and BET specific surface areas than sample ALK. The results are in line with previous reports where $ZnCl_2$ was used as an activating agent to develop micropores on the materials [27,28]. The differences observed in the hysteresis loop of the N_2 isotherms indicate that the samples also have different mesopore sizes. As can be seen in the pore size distributions calculated by QSDFT in Fig. S4a, while LZ promotes the formation of a large volume of mesopores of different sizes from 2.5 to 30 nm, NZ fosters the formation of a much narrower distribution of mesopores with an average diameter of ca. 4.5 nm. The use of LK fosters the formation of a much lower volume of mesopores. Interestingly, as in ALZ sample, ALK exhibits a wide dispersion of mesopore diameters. CO_2 adsorption isotherms (Fig. 2b) corroborate the important differences between the two samples prepared using $ZnCl_2$ and LK. For instance, the amount of CO_2 adsorbed by ANZ and ALZ at 273 K was of 6.6 and 5.6 mmol/g while ALK adsorbs only 2.6 mmol/g. Compared with carbons derived from cytosine [18], the samples prepared using adenine show a larger micropore and mesopore volume. The differences raise the temperature at which the carbonaceous precursor starts condensing, and the interactions between the precursor and the salt melt. The amount of CO_2 adsorbed directly correlated with the calculated narrow microporous volume ($V_{mic,CO2}$) of the samples, that was 0.276, 0.211 and 0.117 cm^3/g for ANZ, ALZ and ALK, respectively. Thus, the results indicate that the amount of narrow micropores also increases by the presence of the transition metal chloride. Pore size distributions according to CO_2 isotherms are not provided as the significant content of heteroatoms may translate into poor reliability of the results [29].

3.1.2. PtRu/ANCs electrocatalysts

At this point, the different adenine-derived noble carbons (ANCs) were used as supports for the synthesis of PtRu-based electrocatalysts through the modified polyol method. Samples containing PtRu nanoparticles were denoted hereafter as PtRu/ANZ,

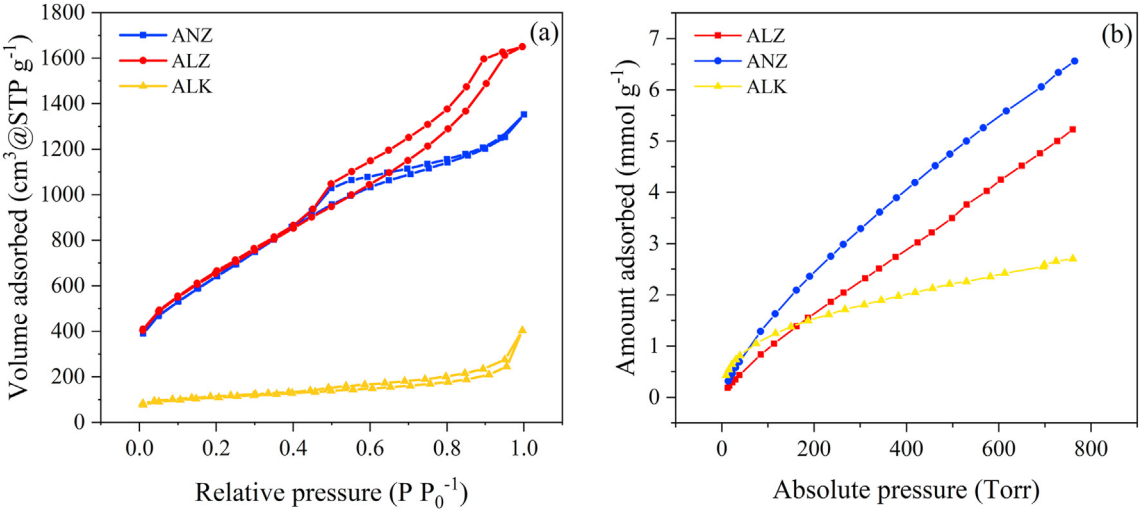

Fig. 2. (a) N_2 adsorption/desorption isotherms at 77 K and (b) CO_2 adsorption/desorption isotherms at 273 K of ALZ, ANZ and ALK.

PtRu/ALZ, PtRu/ALK depending on the ANC material used. The total metal loading was confirmed by ICP measurements reaching nominal values around 60 wt% and 2:1 mass ratio of Pt and Ru for all the synthesized electrocatalysts.

Fig. 3 a depicts the X-ray diffraction (XRD) patterns for all the as-prepared electrocatalysts. The diffraction peaks at 2 θ angles below 35° correspond to the graphitic stacks of the carbonaceous material (mainly for the ALK sample) as previously discussed in Fig. S1b. In general terms, all samples show peaks at 2 θ values around 39.7°, 46.3°, 67.3° and 81.5° which are attributed to the (1 1 1), (2 0 0), (2 2 0) and (3 1 1) planes of the face-centered cubic (fcc) structure of platinum (JCPDS 04–0802). The Ru identification results are difficult through this technique since the main diffraction peaks for this metal (JCPDS 06–0663) overlap with the Pt signal. Despite this, note that a poorly defined peak is observed between the (1 1 1) and (2 0 0) Pt terraces which is associated with the Ru (1 0 1) plane, characteristic of a hexagonal close packed (hcp) structure of Ru. In addition, the absence of any signal of oxidized crystalline species is a preliminary indication of a suitable reduction of the metal phases during the synthesis method. However, their presence should not be totally ignored since they could be found forming very small crystallites or in an amorphous form not being detectable by XRD. The average particle size was estimated according to the Scherer's equation from the Pt (2 2 0) peak (as typically reported) [30]. As expected, all samples showed the formation of very small nanoparticle sizes being in the crystallites range (3–5 nm) to judge by the wide diffraction peaks observed in Fig. 3a. Thus, PtRu/ANZ exhibited the smallest crystallite sizes followed by PtRu/ALZ and PtRu/ALK which presented the largest ones (see Table 2). Compared with pure Pt reflections (dashed lines), right-shifted XRD peaks indicate that Ru has been introduced into the Pt matrix, forming PtRu alloys over the ANC materials [12]. Interestingly, this behavior was mainly observed for the ALZ and ALK-based samples, in particular for this latter, presenting a more accused 2 θ variation (>1.5° for the Pt (2 2 0) plane). Fig. S5 illustrates a zoom of the mentioned region. In contrast, no shift was registered in the PtRu/ANZ pattern suggesting a lower interaction between Pt and Ru nanoparticles. Table 2 summarizes the (2 2 0) peak position, the lattice parameter and the alloy percentage calculated by Vergard's law. According to the decrease in the lattice parameter, the percentage of alloyed ruthenium in the three samples dramatically changes from 0 to 11.5% for PtRu/ANZ and PtRu/ALZ respectively, reaching 58.29% for PtRu/ALK (reverse trend than particle size). Bearing in mind that the deposited active phase (Pt–Ru) was the same for all the electrocatalysts, such variations (size and alloy percentage) are mainly ascribed to the chemical nature and morphology of the different carbonaceous materials. In this context, the use of carbonaceous supports with a high content of mesopores and low surface areas (i.e. ALK) implies the formation of larger nanoparticles and hence, a higher alloy degree due to a less available surface for the nanoparticles deposition. In the case of ANZ and ALZ-based noble carbons, the huge BET surface area presented by these samples (5.5 times higher than ALK) boosted the formation of small nanoparticles mainly for PtRu/ANZ, probably due to the much higher microporous nature of ANZ (corroborated by the N_2 isotherms tests). Therefore, at first glance, a lower nitrogen content and a higher porosity provide a higher dispersion degree and a lower alloy percentage while a lower microporosity nature results in the opposite.

To further evaluate the morphology and crystallite size distribution TEM analyses were performed. Fig. S6 illustrates examples of HRTEM images, and the associated histograms obtained for the different PtRu/ANCs electrocatalysts. Generally, it can be observed a uniform and remarkably high dispersion of metal crystallites on the noble carbon supports. Measurements based on more than 1200 particles count indicate that the average crystallite size was around 2–3.2 nm, being smaller for PtRu/ANZ sample followed by ALZ and ALK-based electrocatalysts (see Table 2). In this sense, PtRu/ANZ and PtRu/ALZ exhibited a much narrower size distributions where around 80 and 60% of the total number of crystallites were between 0.5 and 2.5 nm. Conversely, PtRu/ALK presented more than the 50% of the total count shifted to larger crystallite sizes (3–7 nm), which is associated with a lower dispersion degree and a higher agglomeration. Despite this trend was similar to that obtained by the XRD technique, note that HRTEM estimations were considerably lower than those calculated via Scherer's equation. This discrepancy might arise from the non-well-defined peaks found in the XRD patterns. In addition, it is important to consider that the detection limit of the X-ray diffraction technique is close to 2–3 nm. Fig. S7 shows the elemental mapping images of the Pt, Ru and C elements, presenting a good dispersion as previously demonstrated in the HRTEM images for all materials. Finally, the metal content of the different electrocatalysts were checked through EDX coupled to

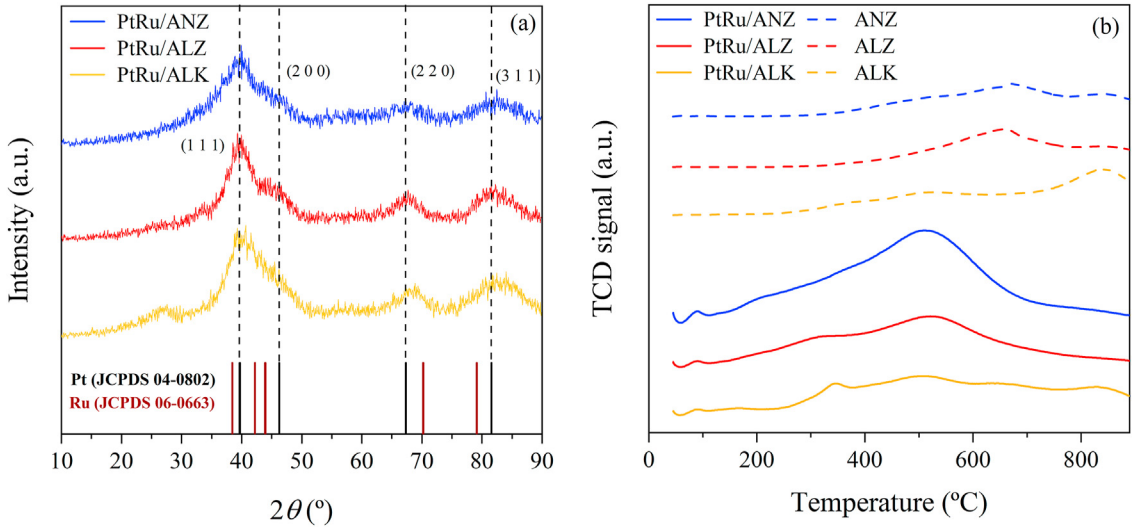

Fig. 3. XRD patterns (a) and TPR spectra (b) for the different PtRu/ANCs.

Table 2
Summary of nanoparticles dimension and nature extracted from XRD patterns and from TEM micrographs.

Sample	Particle size (nm)		Lattice parameter (nm)	Pt (220) position (2θ)	Alloyed Ru (%)
PtRu/ANZ	3.7[a]	2.0 ± 0.4[b]	0.3930	67.34	0
PtRu/ALZ	4.8[a]	2.7 ± 0.5[b]	0.3911	67.70	11.54
PtRu/ALK	5.5[a]	3.1 ± 0.8[b]	0.3853	68.86	58.29

[a] From XRD using Scherrer equation.
[b] From TEM micrographs.

HRTEM confirming a total loading close to 60 wt % and 2:1 of mass ratio for all cases (Table S3).

To clarify the chemical state of Pt and Ru in the polyol-synthesized electrocatalysts, temperature-programmed reduction (TPR) experiments were carried out (Fig. 3b). Profiles of the noble carbon supports before the nanoparticles deposition were also shown for comparison purposes. For the carbonaceous materials, different hydrogen consumption peaks were registered at high temperature levels (>500 °C) assigned to the gasification process of the fresh supports. In the case of the PtRu/ANCs samples, various minor peaks were observed at low temperature interval (0–200 °C). These peaks are attributed to the desorption of H_2 previously adsorbed on the Pt surface (initial negative peaks) [31] and/or to the presence of small traces of Pt oxides on the catalyst surface [32]. However, to judge by the low intensity of the signal and considering the absence of crystalline PtO_2 species in the XRD profiles, it is possible to confirm an efficient reduction of the Pt precursors during the synthesis method. Subsequently, a group of different reduction peaks can be observed between 200 and 450 °C for all the PtRu/ANCs electrocatalysts. According to the available literature [33,34], such hydrogen consumption peaks are attributed to the presence of Ru^aO_2 species in an amorphous state (not detectable by XRD) which could be present isolated or on the surface of the PtRu alloy. In addition, the formation of Ru^cO_2 (crystalline phases) results difficult through the polyol method since these species are normally promoted under the application of high temperatures air post-treatment (>500 °C) [35]. On the other hand, note that the Ru^aO_2 peak area decreases for samples with a higher alloying degree (i.e. PtRu/ALK) which suggests that Ru is in metal state when it is introduced into the Pt lattice. Finally, peaks centered at 500 °C are assigned to the carbonaceous material decomposition. By comparing with the fresh support profiles, the intensity of these peaks considerably increases after the active phase deposition, indicating that the metal nanoparticles catalyze the support gasification. This behavior was more noticeable for the PtRu/ANZ sample probably due to the higher dispersion degree (smaller crystallites sizes) being in good agreement with the XRD-TEM results.

The textural analysis of the electrocatalysts using N_2 isotherms at 77 K and CO_2 isotherm at 273 K is shown in Fig. 4. BET specific surface area of PtRu/ANZ, PtRu/ALZ, and PtRu/ALK drop from 2,292 m^2/g, 2,334 m^2/g and 389 m^2/g to 743 m^2/g, 900 m^2/g and 234 m^2/g, respectively (see Table 3). Here, it is important to consider that the amount of metal nanoparticles in the samples makes the specific surface area differ from the original value by a 60% (i.e. the wt% loading of metal). Interestingly, PtRu/ALK shows virtually the expected specific surface area (i.e. 234 m^2/g vs. the theoretical 233 m^2/g – 60% of 389 m^2/g). On the other hand, samples PtRu/ANZ, PtRu/ALZ show a much lower value than the expected (i.e. 1,375 m^2/g and 1,400 m^2/g), which points at their porosity helping on the dispersion of PtRu nanoparticles. The virtually unchanged isotherms shape and QSDFT pore size distributions after metals deposition indicate that the remaining open pores are not blocked by the nanoparticles (Fig. 4 and Fig. S4b). CO_2 sorption measurements at 273 K are in consonance with the partial blockage of pores observed by N_2 sorption measurements at 77 K. Again, PtRu/ALZ and PtRu/ANZ show the largest decrease in the calculated total pore volume (i.e. from 0.211 cm^3/g to 0.276 cm^3/g to 0.105 and 0.074 cm^3/g, respectively) as can be seen in Table 3. On the other hand, PtRu/ALK shows a lower decrease in the CO_2 sorption from 0.117 to 0.1 cm^3/g.

3.2. Electrochemical characterization in a three electrodes cell

Redox properties of the different PtRu/ANCs were studied by cyclic voltammetry (CV) essays at room temperature in absence of ethanol. Fig. 5 a shows the CV profiles in N_2 saturated electrolyte (0.25 M $HClO_4$ aqueous solution) in the potential range of −0.038 to 1.4 V vs. RHE using a sweep rate of 50 mV/s. The cyclic voltammograms displayed the typical features of the Pt-based electrocatalysts with the hydrogen adsorption/desorption region, the double layer charge and the oxidation/reduction of the Pt surface [36]. Various hydrogen desorption peaks were observed in the forward scan for all the synthesized electrocatalysts which are

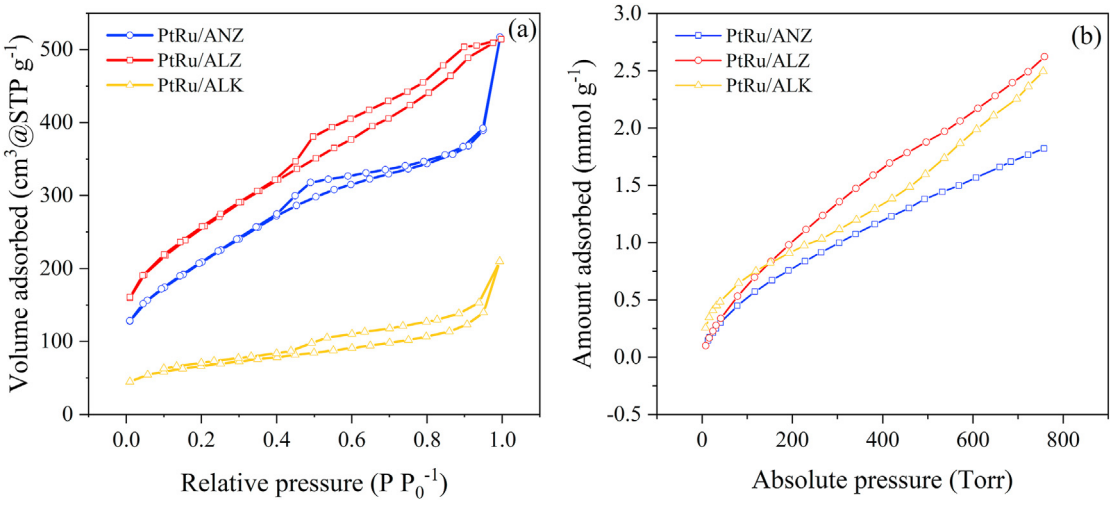

Fig. 4. (a) N_2 adsorption/desorption isotherms at 77 K and (b) CO_2 adsorption/desorption isotherms at 273 K of PtRu/ALZ, PtRu/ANZ and PtRu/ALK.

Table 3
Summary of the physicochemical parameters obtained for the different PtRu/ANCs by N_2 adsorption-desorption isotherms at 77 K and CO_2 adsorption-desorption isotherms at 273 K.

Sample	S_{BET} (m^2/g)[a]	V_{T,N_2} (cm^3/g)[b]	V_{mic,CO_2} (cm^3/g)[c]
PtRu/ANZ	743	0.60	0.074
PtRu/ALZ	900	0.79	0.105
PtRu/ALK	234	0.22	0.099

[a] Specific surface area was calculated from nitrogen adsorption data (P/P0 < 0.2) using the Brunauer-Emmett-Teller (BET) method.
[b] Total pore volume (V_T) was calculated from the amount of nitrogen adsorbed at P/P0 = 0.995.
[c] Total micropore volume was calculated from the amount of carbon dioxide adsorbed at 730 Torr.

associated with a particular orientation of Pt terraces. Peaks centered at 0.05 V vs. RHE are attributed to Pt (1 1 0)-types sites while peaks between 0.1 and 0.35 V vs. RHE are associated with the hydrogen adsorption/desorption on Pt (1 0 0) planes [37]. Among the different samples, the intensity variation of the hydrogen desorption peaks reveals changes on the nanoparticles surface. Thus, PtRu/ANZ showed a preferential orientation of the Pt (1 0 0) domains as the second peak area was higher. In contrast, ALZ and ALK-based electrocatalysts presented a more prominent peak at 0.05 V which indicates a higher density of Pt (1 1 0)-type sites. To estimate the amount of active sites, the electrochemical active surface area (ECSA) was calculated through the hydrogen adsorption/desorption region. Accordingly, the ECSA value for PtRu/ANZ (34.06 m^2/g) was found to be the highest compared to PtRu/ALZ (28.84 m^2/g) and PtRu/ALK (15.58 m^2/g). This is attributed to the smaller crystallite size and the more uniform dispersion of the PtRu nanoparticles supported on ANZ, which demonstrates a superior synergic interaction between the active phase and this noble carbon support. In addition, note that ECSA values decrease as the alloy percentage between Pt and Ru is higher (PtRu/ALK > PtRu/ALZ > PtRu/ANZ), indicating that a significant alteration of the Pt structure could considerably decrease the Pt active sites (mainly Pt (1 0 0) domains). It also explains the dramatical ECSA drop when the ALK support is used although the crystallite size difference is not very significant, being the ECSA variation proportional to the rise of the alloying degree. On the other hand, the degradation degree of the synthesized electrocatalysts was explored by ADT at the same conditions mentioned previously (Fig. S8). It was estimated from the ECSA variation between 1st and 500th cycles (Table S4). As it can be observed, a decrease in the hydrogen desorption peak associated with the Pt (1 0 0)-types sites is registered while that related to Pt (1 1 0)-planes suffers a slight increase. This change of the Pt orientated terraces might be accounted for the Pt and Ru redeposition/sintering process with the consequent metallic species migration through the catalyst surface (Ostwald ripening effect) [38]. Regarding the degradation degree, all samples exhibited values within an interval between 7 and 35%, well below those obtained for similar active metals supported on other carbonaceous materials such as carbon Vulcan or carbon black (40–60% of degradation) [5]. In this sense, it seems that the high surface area and large nitrogen content provided by the noble carbon materials could prevent the sintering process, decreasing the degradation of the catalyst for long-term applications.

To further assess the electrochemical performance of PtRu/ANCs electrocatalysts, additional CVs were carried out using a 4 M EtOH + 0.5 M $HClO_4$ aqueous solution saturated with a N_2 stream within the potential window of 0–1.2 V vs. RHE at a scan rate of 10 mV/s. Same tests were accomplished for the fresh noble carbon supports (not shown here) obtaining a negligent current density which proves that these materials are not active before the nanoparticles deposition. The CV profiles (Fig. 5b) displayed the typical behavior of the ethanol oxidation possessing one prominent anodic peak in the forward scan around 1.1 V vs. RHE, and another in the backward scan between 0.8 and 1 V vs. RHE. The anodic peak in the positive direction is generated due to the electrocatalytic oxidation of ethanol to intermediate products [39]. On the other hand, the peak observed during the reverse scan is associated with the oxidation of intermediate species derived from the partial oxidation as well as with the re-starting of the ethanol oxidation after the reduction of the Pt oxide (re-activation of the catalyst surface) [40]. Table 4 summarizes the different EOR parameters extracted from the CV essays. From Fig. 5b, the onset potential was found to follow the order PtRu/ANZ (0.45 V vs RHE) < PtRu/ALZ (0.51 V vs RHE) < PtRu/ALK (0.7 V vs RHE) indicating a promoted ethanol oxidation on the ANZ-based electrocatalyst at low polarization levels (low activation energy). The maximum current density obtained from the forward peak is normally used to describe the electrocatalytic activity toward the EOR process. In general terms, a remarkable difference in the electrochemical performance for the diverse synthesized materials can be observed. Thus, PtRu/ANZ (28 mA/cm^2) exhibited the largest current density in the whole potential interval followed by PtRu/ALZ (18.9 mA/cm^2) and PtRu/ALK (6.3 mA/cm^2). In addition, quite defined ethanol oxidation peaks were obtained for ANZ and ALZ-based electrocatalyst while PtRu/ALK presented a broad CV profile suggesting a poor electrocatalytic activity. Current density values were also normalized against the PtRu total loading (mass activity) and respect to the ECSA values (specific activity), as shown in Fig. 5c. The mass activity of PtRu/ANZ reached values of around 440 mA/mg_{PtRu} being 1.5 and 4.4 times higher than PtRu/ALZ and PtRu/ALK, respectively. A similar behavior was observed for the specific activity. Considering that the active phase and metal loading were the same for all the as-prepared materials, the variation in the electrochemical performance could be explained attending to different factors. Based on the physicochemical characterization, PtRu/ANZ presents smaller crystallite sizes and hence, a higher dispersion degree compared to the rest of electrocatalysts, which increases the Pt utilization. Alloying degree is another parameter to consider since it considerably varies depending on the support (58%, 12% and ~ 0% for PtRu/ALK, PtRu/ALZ and PtRu/ANZ, respectively). Although it is well known that the PtRu alloy formation promotes ethanol electrooxidation via water dissociation (OH^- species formation) [41], an excessive alteration of the electrocatalyst surface could decrease the Pt active sites availability [18]. This is the case of PtRu/ALK where the limited ECSA could hinder the ethanol adsorption/dissociation process. The crystallinity and porosity of the supports template also play an essential role in the EOR development. According to the XRD and porosity studies, ANZ and ALZ present large BET surfaces areas but differ in the microporosity degree (ANZ > ALZ), while ALK exhibits a lower pore volume and increased graphitic stacks. This more developed porosity is beneficial to promote reactant/products flow channels during the electrochemical process which could maximize the EOR activity (mainly for PtRu/ANZ) [42]. In contrast, highly graphitic carbonaceous materials (i.e. ALK) are not preferable for ethanol oxidation, since their worse porous structure hinders the access of the reactant to the catalytic active sites concluding that a minimum porosity is mandatory to obtain a good electrochemical performance [14]. Finally, it should be noted that the PtRu/ANZ also presents the highest specific activity which reveals that the intrinsic activity per active site (i.e. isolated trend from the ECSA) is higher for this electrocatalyst. This can be explained attending to the type and nature of the Pt oriented monocrystals. Previous studies have proved that the ethanol

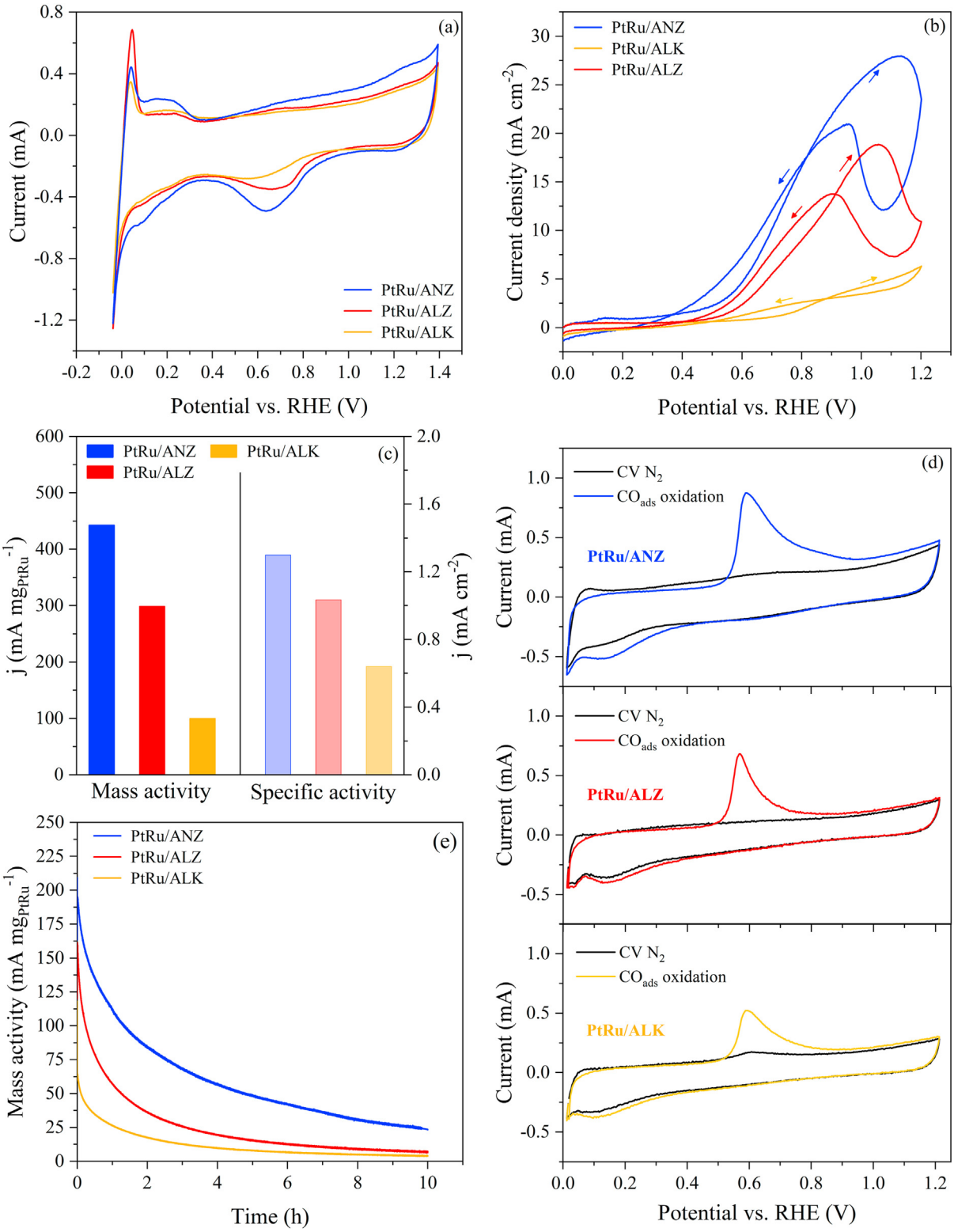

Fig. 5. EOR performance of the PtRu electrocatalysts supported on different adenine derived noble carbons. a) CVs curves in N_2-saturated 0.25 M $HClO_4$ solution at scan rate of 50 mV/s. b) CVs profiles in N_2-saturated 4 M ethanol + 0.5 M $HClO_4$ solution at scan rate of 10 mV/s. c) Electrocatalytic activity from b) normalized by metal loading and ECSA values. d) CO-stripping curves in N_2-saturated 0.5 M $HClO_4$ electrolyte at 20 mV/s. e) Chronoamperometry tests at fixed potential of 0.7 V vs. RHE for 10 h.

oxidation process is a structure-sensitive reaction, where the Pt (1 0 0) basal plane (PtRu/ANZ > PtRu/ALZ > PtRu/ALK) is the one that results in the highest current density [43–45]. In this sense, the enhanced overall current density provided by PtRu/ANZ was due to the contribution of both an enhanced Pt utilization and more selective active sites, boosting the EOR performance.

To evaluate the ability of poisoning intermediates removal, CO stripping experiments were carried out in absence of ethanol using

Table 4
Electrochemical parameters for the EOR. Electrochemical active surface area (ECSA), onset potential (E_o), forward and backward peak potentials (E_f and E_b), forward and backward peak current density (I_f and I_b), mass activity and specific activity.

Catalyst	ECSA (m^2/g)	Potential (V)			Current density (mA/cm^2)		Mass activity (mA/mg_{PtRu})	Specific activity (mA/cm^2)
		E_o	E_f	E_b	I_f	I_b		
PtRu/ANZ	34.06	0.45	1.12	0.95	27.95	20.94	442.5	1.30
PtRu/ALZ	28.84	0.51	1.06	0.90	18.85	13.75	298.5	1.03
PtRu/ALK	15.58	0.70	–	–	6.30	–	99.75	0.64

a 0.5 M $HClO_4$ electrolyte (Fig. 5d). CVs in N_2 saturation are also shown for comparison purposes. The CO oxidation onset potentials for PtRu/ALZ and PtRu/ANZ (0.497 V and 0.507, respectively) were more negative compared to that for PtRu/ALK (0.527 V) demonstrating a more efficient CO removal for ALZ and ANZ based electrocatalyst. Furthermore, the peak area associated with the CO oxidation process followed the sequence PtRu/ANZ > PtRu/ALZ > PtRu/ALK which is indicative of a higher Pt active sites availability when ANZ noble carbon is used (same trend as that obtained for ECSA values).

The durability of the prepared samples was also examined by chronoamperometric measurements at a fixed potential of 0.7 V vs. RHE in N_2 saturated 4 M EtOH + 0.5 M $HClO_4$ solution for 10 h as shown in Fig. 5e. The preliminary sharp decay in the current density was attributed to the double layer charging. Subsequently, a gradual drop of the electrocatalytic activity was detected due to the poisoning effect of active sites by intermediate species along with the generation of oxides and hydroxides on the metal surface during the ethanol oxidation [39]. A pseudo steady state was attained after a few hours, obtaining a positive current density for all electrocatalysts after 10 h of operation. Once again, PtRu supported on ANZ presents the best electrochemical performance being in consonance with the ECSA and mass activity results.

Once the differences between the PtRu/ANCs were elucidated and in order to prove the real advantage of the adenine-derived noble supports against the typical Vulcan XC-72, additional CVs essays using PtRu/C were conducted (Fig. S9). The CVs comparison shows a clear outstanding performance by the noble carbon materials, being the mass activity of ANZ and ALZ-based electrocatalyst 2.4 and 1.6 times higher than that obtained for PtRu/C. Such enhancement of the EOR performance might be accounted for different aspects: (i) the surface area of the noble carbons supports is extremely high (2,000 m^2/g), around 10 times higher than that of the carbon Vulcan (200–250 m^2/g). This results in a better metals dispersion and allows the formation of smaller crystallites sizes (∼ 2 nm for PtRu/ANCS and between 4 and 6 nm for PtRu/C as typically reported [5,46]) preventing the sintering effect. (ii) As proved in our previous study concerning cytosine-derived carbons for electrochemistry applications [18], these carbonaceous materials act as a noble material providing a higher resistance upon oxidation which increases the stability at high potentials levels. (iii) The synthesis procedure and the precursors used allow the obtention of a carbonaceous material with a relatively high nitrogen content (14–30%). Literature review reveals that nitrogen doping in carbon nanostructures can improve the electrocatalytic activity toward both methanol and ethanol oxidation [47,48]. In summary, the incorporation of N-species into the carbon network facilitates the electrons transfer process increasing the electrical conductivity of the material [49]. Also, it provides surface defects which are beneficial to anchor the Pt nanoparticles improving the electrocatalytic performance [42]. Finally, a comparison with other Pt-based electrocatalysts supported on different materials is presented in Table S5. Among all the reported electrocatalysts, the activity of PtRu/ANCs was the highest toward the EOR confirming the excellent performance of the adenine-based noble carbon supports mainly for PtRu/ANZ. Furthermore, it should be highlighted that most of these studies evaluate the electrochemical performance at more advantageous scan rate conditions (20–50 mV/s instead of 10 mV/s used in this work) which entails a reduced poisoning effect due to the intermediate species have less time to form and block the electrocatalyst surface [50]. In this sense, the performance gap would be even higher demonstrating the clear advantages of the herein proposed materials.

All electrochemical parameters considered, ANZ and ALZ-based electrocatalysts were selected as the best anodes (superior activity compared to PtRu/C) for the subsequent scale-up of the system to a PEM cell configuration.

3.3. Ethanol electro-reforming in a proton exchange membrane (PEM) cell

3.3.1. Electrochemical measurements

The ethanol electrochemical reforming process was explored in a two compartments cell (PEM electrolyzer) using the selected PtRu/ANCs as anodic electrocatalysts. Firstly, linear sweep voltammetry tests were conducted in a potential range from 0 to 1.4 V, at 80 °C and at a scan rate of 20 mV/s for a 4 M ethanol inlet stream (Fig. 6a). In line with the half-cell experiments, PtRu/ANZ provided the best electrocatalytic activity, showing a more negative onset potential (0.28 V) and a higher current density value (512 mA/cm^2 at 1.4 V) than those obtained for PtRu/ALZ (0.38 V and 431 mA/cm^2). At high potential levels (>1 V), a slight drop in the curve slope of the LSV profiles can be observed for both samples. This is attributed to small diffusional limitations which mainly take place in the high polarization interval (high conversion) since the system starts to be controlled by mass transfer resistance instead of kinetics limitations. Nevertheless, remarkable current density values were obtained for both electrocatalysts compared to the typical values observed for ethanol electroreforming based on MEAs. For instance, previous works have shown that using PtRu/C-Nafion-Pt/C and PtSn/C-Nafion-Pt/C MEAs, current densities below 150 mA/cm^2 were obtained under similar operating conditions and acid media [51,52]. In addition, the electrocatalytic activity reached was even similar to that obtained in membrane-less electrolyzers based on Pd/C in basic media (450 mA/cm^2 at 1.4 V and 10 mV/s) [53], which proves the efficiency of the PtRu/ANCs electrocatalyst also in a single-cell configuration.

To further study the electrochemical performance, galvanostatic transients were carried out from 0.2 to 1.2 A (i.e. 40–240 mA/cm^2) maintaining each current step for 15 min. Fig. 6b illustrates the potential vs. time on stream at 80 °C and 4 M ethanol. Also, note that the assay was aborted when the potential exceeded 1.5 V in order to avoid the simultaneous water electrolysis. In general terms, PtRu/ANZ required the lowest cell potential in the whole interval of study, being in consonance with the LSV experiments. At moderate galvanostatic levels (0.2–0.6 A), both anodes exhibited a very stable profile attaining a steady-state potential after a few seconds on stream, which is indicative of the good stability of the

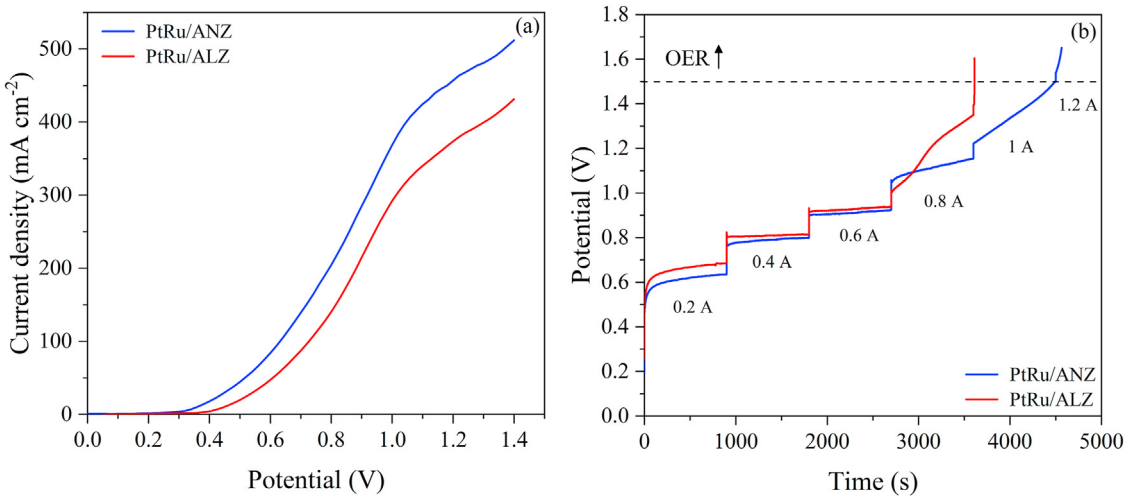

Fig. 6. Ethanol electroreforming assays using a PEM electrolysis cell at 80 °C for a 4 M ethanol inlet stream (1.15 mL/min). a) LSV profiles between 0 and 1.4 V using a scan rate of 20 mV/s. b) Galvanostatic transients between 0 and 1.2 A.

system. In contrast, for a higher demanded current, a slight increase of the cell potential was detected for PtRu/ANZ being much sharper for ALZ-based anode, which leads to a rapid loss of the electrocatalytic activity in the subsequent levels (>1 A). Such behavior could be associated with the mass transfer limitations, which are more accentuated for PtRu/ALZ, probably due to its limited active sites availability compared to PtRu/ANZ. Furthermore, at very high overpotentials, hydroxyl species adsorbed on the catalyst surface could increase the coverage degree competing with the ethanol adsorption and leading to a partial deactivation. Therefore, a

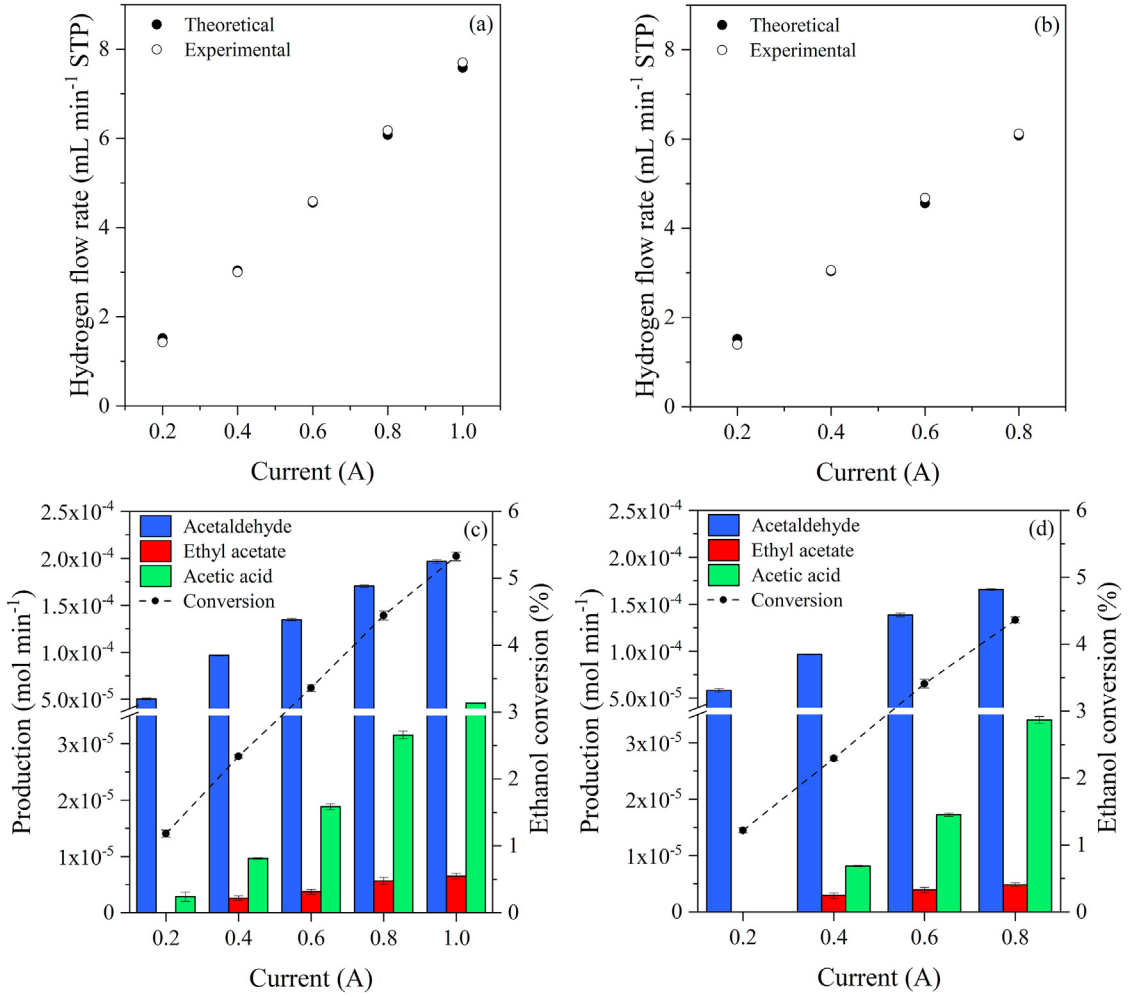

Fig. 7. Product distribution at different galvanostatic levels. (i) Experimental hydrogen measurements of PtRu/ANZ (a) and PtRu/ALZ (b). (ii) Organic compounds molar rates and ethanol conversion of PtRu/ANZ (c) and PtRu/ALZ (d).

maximum current operation of 0.8 A (160 mA/cm^2) and 1 A (200 mA/cm^2) was reached for PtRu/ALZ and PtRu/ANZ, respectively, before overlapping with the oxygen evolution reaction (OER) interval. To evaluate the electrocatalytic activity after the chronopotentiometry (CP) measurements, additional LSV were carried out (Fig. S10). A slight decrease of the current density (<10%) was registered at high potential range (>1 V) associated with the poisoning species due to the previous continuous operation. Nevertheless, note that the obtained profiles are identical at lower potential range (0–1 V), confirming a suitable stability of the metal species and the noble carbon supports.

3.3.2. Products distribution and energy consumption

In order to achieve more insight into ethanol electroreforming and to demonstrate the potential of this technology for green chemical generation, the analysis of the product distribution was carried out. Fig. 7 shows the hydrogen and organic compounds production along with the ethanol conversion for the different PtRu/ANCs anodes at each galvanostatic step (0.2–1 A). Hydrogen production rates were measured from the cathodic effluent accumulated for each applied current stage and compared with those values calculated via Faraday's law. As expected, experimental hydrogen data perfectly fit with the theoretical ones, confirming a hydrogen faradaic efficiency close to 100% for both anodes (Fig. 7a–b). Regarding the anodic performance, the interpretation of the results is more difficult since the EOR follows a complex reaction mechanism leading to the generation of several by-products (acetaldehyde, acetic acid, carbon dioxide, among others). However, a recent work about the EOR reaction mechanism using polymeric membrane cells has proved that at the present operating conditions (high ethanol concentration and cell potentials), product distribution is shifted toward acetaldehyde and acetic acid pathways limiting the generation of gaseous products (CO_2 or CH_4) [54]. Furthermore, the hydrodynamic conditions of the PEM cell hinder even more the production of these latter compounds. In this basis, acetaldehyde was obtained as the major compound followed by acetic acid and ethyl acetate (Fig. 7c–d). Equations S1–S6 of the supplementary information depict the complete mechanism for a PtRu catalyst. Accordingly, ethanol oxidation takes place following a bifunctional mechanism where ethanol adsorption and acetaldehyde generation mainly occur on the Pt surface, while Ru provides an efficient water dissociation leading to the acetic acid production. Therefore, a more boosted acetic acid production implies a higher development of the oxidation process. To judge by the mole production rates, PtRu/ANZ exhibits a higher selectivity toward acetic acid than PtRu/ALZ in almost all the interval of study except for the 0.8 A level. The discrepancy observed at 0.8 A is attributed to the higher cell potential required for PtRu/ALZ electrocatalyst compared to PtRu/ANZ (see Fig. 6b) since the OH^- species generation is promoted at much higher overpotentials. In this sense, it is possible to confirm a higher number of transferred electrons for PtRu/ANZ or in other words, a higher intrinsic activity (in line with the half-cell essays). The faradaic efficiency of the EOR is shown in Fig. S11. In general terms, an overall faradaic efficiency close to 100% was obtained for all current levels which demonstrates that no additional products have formed in the anodic chamber of the cell. In addition, note that, at higher polarization levels, the faradaic efficiency corresponding to acetic acid increased being in consonance with the product distribution trend. Concerning ethanol conversion rates per cell pass, both anodes presented similar results reaching values up to 4.36% for PtRu/ALZ and 5.33% for PtRu/ANZ which correspond with the maximum galvanostatic performance provided for each electrocatalyst (180 and 200 mA/cm^2, respectively).

Table 5
Energy requirements of each anode extracted from the galvanostatic transient tests.

Catalyst	Current (A)	Current density (mA/cm^2)	V_m[a] (V)	Power (W)	Consumption (kWh/kgH_2)
PtRu/ANZ	0.2	40	0.61	0.12	16.33
	0.4	80	0.79	0.32	21.13
	0.6	120	0.91	0.55	24.42
	0.8	160	1.11	0.89	29.80
	1.0	200	1.35	1.35	36.24
PtRu/ALZ	0.2	40	0.66	0.13	17.60
	0.4	80	0.81	0.32	21.68
	0.6	120	0.93	0.56	24.86
	0.8	160	1.19	0.95	31.93
	1.0	200	>1.5	–	–

[a] Average potential estimated from each applied current step.

Finally, the energy requirements to produce 1 kg of hydrogen at each applied current step were estimated and collected in Table 5. According to the potential vs. time profile, PtRu/ANZ presented the lowest consumption over the entire range tested being the differences more patent at high demanded current values. Despite this, both anodes present energy requirements well below those reported for commercial water PEM electrolyzers (50–60 kWh/kgH_2) [55,56].

4. Conclusions

Three different adenine-based noble carbons were synthesized by using various salt mixtures and subsequently used for the preparation of PtRu electrocatalysts. The use of different salt templating agents during the synthesis method caused a variation in the support structure and hence, in the final electrocatalyst morphology. In general terms, a more developed microporosity and a larger surface area led to the formation of smaller nanoparticles and a higher dispersion degree, which translated into a higher ECSA and a superior electrocatalytic activity toward the EOR. In contrast, carbonaceous materials with a poor porosity degree and a high graphitic nature fostered the formation of larger nanoparticles and a higher alloying degree, which decreased the Pt availability. PtRu/ANZ electrocatalyst exhibited the best electrochemical performance in both half-cell and PEM cell configurations. In addition, the use of this catalytic support resulted to be more efficient than the typical carbon Vulcan, reaching an electrocatalytic activity around 2.4 times superior compared to PtRu/C. This was attributed to different aspects such as the elemental composition of the support (larger nitrogen content and stability), a higher dispersion degree and a more basic nature of these materials providing better anchorage points for the metal nanoparticles.

Credit author statement

A. Rodríguez-Gómez: Conceptualization, Data curation, Formal Analysis, Investigation, Methodology, Validation, Visualization, Writing-original draft and Writing-review and editing. **E. Lepre:** Data curation, Formal Analysis, Methodology, Investigation, Visualization and Writing-original draft. **F. Dorado:** Writing-review and editing. **L. Sánchez-Silva:** Writing-review and editing. **N. López-Salas**: Writing-review and editing. **A.R. de la Osa**: Conceptualization, Visualization, Writing-Reviewing, Supervision.

Data availability

The authors are unable or have chosen not to specify which data has been used.

Declaration of competing interest

The authors declare that they have no known competing financial interests or personal relationships that could have appeared to influence the work reported in this paper.

Acknowledgments

We gratefully acknowledge the Spanish Ministry of Science and Innovation (State Research Agency. Project PID2019-107499RB-100) for the financial support. The Max Planck Society is gratefully acknowledged for financial support.

Appendix A. Supplementary data

Supplementary data to this article can be found online at https://doi.org/10.1016/j.mtener.2022.101231.

References

[1] Z. Zhu, N. Sathitsuksanoh, T. Vinzant, D.J. Schell, J.D. McMillan, Y.H. Zhang, Comparative study of corn stover pretreated by dilute acid and cellulose solvent-based lignocellulose fractionation: enzymatic hydrolysis, supramolecular structure, and substrate accessibility, Biotechnol. Bioeng. 103 (2009) 715–724.
[2] Y.X. Chen, A. Lavacchi, H.A. Miller, M. Bevilacqua, J. Filippi, M. Innocenti, A. Marchionni, W. Oberhauser, L. Wang, F. Vizza, Nanotechnology makes biomass electrolysis more energy efficient than water electrolysis, Nat. Commun. 5 (2014) 4036. https://www.nature.com/articles/ncomms5036?origin=ppub.
[3] C. Manochio, B.R. Andrade, R.P. Rodriguez, B.S. Moraes, Ethanol from biomass: a comparative overview, Renew. Sustain. Energy Rev. 80 (2017) 743–755.
[4] H.A. Miller, A. Lavacchi, F. Vizza, Storage of renewable energy in fuels and chemicals through electrochemical reforming of bioalcohols, Curr. Opin. Electrochem. 21 (2020) 140–145.
[5] A. Rodríguez-Gómez, F. Dorado, A. de Lucas-Consuegra, A.R. de la Osa, Influence of Pt/Ru anodic ratio on the valorization of ethanol by PEM electrocatalytic reforming towards value-added products, J. Energy Chem. 56 (2021) 264–275.
[6] A. Rodríguez-Gómez, F. Dorado, P. Sánchez, A.R. de la Osa, Boosting hydrogen and chemicals production through ethanol electro-reforming on Pt-transition metal anodes, J. Energy Chem. 70 (2022) 394–406.
[7] A.R. de la Osa, A.B. Calcerrada, J.L. Valverde, E.A. Baranova, A. de Lucas-Consuegra, Electrochemical reforming of alcohols on nanostructured platinum-tin catalyst-electrodes, Appl. Catal. B Environ. 179 (2015) 276–284.
[8] O.A. Petrii, Pt-Ru electrocatalysts for fuel cells: a representative review, J. Solid State Electrochem. 12 (2008) 609–642.
[9] S. Zhao, H. Yin, L. Du, G. Yin, Z. Tang, S. Liu, Three dimensional N-doped graphene/PtRu nanoparticle hybrids as high performance anode for direct methanol fuel cells, J. Mater. Chem. 2 (2014) 3719–3724.
[10] X. Liu, L. Jiang, Z. Zhu, S. Chen, Y. Dou, P. Liu, Y. Wang, H. Yin, Z. Tang, H. Zhao, Wet-chemistry grafted active pyridinic nitrogen sites on holey graphene edges as high performance ORR electrocatalyst for Zn-Air batteries, Mater. Today Energy 11 (2019) 24–29.
[11] J. Ji, Y. Hou, S. Zhou, T. Qiu, L. Zhang, L. Ma, C. Qian, S. Zhou, C. Liang, M. Ling, Oxygen-coordinated Low-nucleus Cluster Catalysts for Enhanced Electrocatalytic Water Oxidation, Carbon Energy, 2022, pp. 1–11. https://onlinelibrary.wiley.com/doi/full/10.1002/cey2.216.
[12] A.K. Choudhary, H. Pramanik, Addition of rhenium (Re) to Pt-Ru/f-MWCNT anode electrocatalysts for enhancement of ethanol electrooxidation in half cell and single direct ethanol fuel cell, Int. J. Hydrogen Energy 45 (2020) 13300–13321.
[13] Y. Wei, X. Zhang, Z. Luo, D. Tang, C. Chen, T. Zhang, Z. Xie, Nitrogen-doped carbon nanotube-supported Pd catalyst for improved electrocatalytic performance toward ethanol electrooxidation, Nano-Micro Lett 9 (2017) 28. https://link.springer.com/article/10.1007/s40820-017-0129-5.
[14] D. Sebastián, I. Suelves, E. Pastor, R. Moliner, M.J. Lázaro, The effect of carbon nanofiber properties as support for PtRu nanoparticles on the electrooxidation of alcohols, Appl. Catal. B Environ. 132–133 (2013) 13–21.
[15] D.W. Wang, D. Su, Heterogeneous nanocarbon materials for oxygen reduction reaction, Energy Environ. Sci. 7 (2014) 576–591.
[16] J. Serrano-Jiménez, A.R. de la Osa, A. Rodríguez-Gómez, P. Sánchez, A. Romero, A. de Lucas-Consuegra, Graphene-like materials as an alternative to carbon Vulcan support for the electrochemical reforming of ethanol: towards a complete optimization of the anodic catalyst, J. Electroanal. Chem. 921 (2022) 116680. https://www.sciencedirect.com/science/article/pii/S1572665722006725.
[17] M. Antonietti, M. Oschatz, The concept of "noble, heteroatom-doped carbons," their directed synthesis by electronic band control of carbonization, and applications in catalysis and energy materials, Adv. Mater. 30 (2018), 1706836.
[18] A. Rodríguez-Gómez, E. Lepre, L. Sánchez-Silva, N. López-Salas, A.R. de la Osa, PtRu nanoparticles supported on noble carbons for ethanol electrooxidation, J. Energy Chem. 66 (2022) 168–180.
[19] J. Kossmann, D. Piankova, N.V. Tarakina, J. Heske, T.D. Kühne, J. Schmidt, M. Antonietti, N. López-Salas, Guanine condensates as covalent materials and the concept of cryptopores, Carbon 172 (2021) 497–505.
[20] J. Kossmann, T. Heil, M. Antonietti, N. Lopez-Salas, Guanine-Derived Porous Carbonaceous Materials: towards C_1N_1, ChemSusChem 13 (2020) 6643–6650. https://chemistry-europe.onlinelibrary.wiley.com/doi/full/10.1002/cssc.202002274.
[21] W. Yang, T.-P. Fellinger, M. Antonietti, Efficient metal-free oxygen reduction in alkaline medium on high-surface-area mesoporous nitrogen-doped carbons made from ionic liquids and nucleobases, J. Am. Chem. Soc. 133 (2011) 206–209.
[22] J. Pampel, T.P. Fellinger, Opening of bottleneck pores for the improvement of nitrogen doped carbon electrocatalysts, Adv. Energy Mater. 6 (2016), 1502389.
[23] A. Rodríguez-Gómez, F. Dorado, A. de Lucas-Consuegra, A.R. de la Osa, Influence of the GDL and assembly mode of a PEM cell on the ethanol revalorization into chemicals, Chem. Eng. J. 402 (2020) 125298. https://www.sciencedirect.com/science/article/pii/S1385894720312900.
[24] N. Díez, A.B. Fuertes, M. Sevilla, Molten salt strategies towards carbon materials for energy storage and conversion, Energy Storage Mater. 38 (2021) 50–69.
[25] Z.-Y. Wu, S.-L. Xu, Q.-Q. Yan, Z.-Q. Chen, Y.-W. Ding, C. Li, H.-W. Liang, S.-H. Yu, Transition metal–assisted carbonization of small organic molecules toward functional carbon materials, Sci. Adv. 4 (2018), eaat0788.
[26] S.S. Shinde, C.H. Lee, J.Y. Yu, D.H. Kim, S.U. Lee, J.H. Lee, Hierarchically designed 3D holey C_2N aerogels as bifunctional oxygen electrodes for flexible and rechargeable Zn-air batteries, ACS Nano 12 (2018) 596–608.
[27] M. Molina-Sabio, F. Rodrıguez-Reinoso, Role of chemical activation in the development of carbon porosity, Colloids Surf. A Physicochem. Eng. Asp. 241 (2004) 15–25.
[28] A. Ahmadpour, D.D. Do, The preparation of active carbons from coal by chemical and physical activation, Carbon 34 (1996) 471–479.
[29] V. Cornette, J. Villarroel-Rocha, K. Sapag, R. Delgado Mons, J.P. Toso, R.H. López, Insensitivity in the pore size distribution of ultramicroporous carbon materials by CO_2 adsorption, Carbon 168 (2020) 508–514.
[30] L.M. Palma, T.S. Almeida, A.R. de Andrade, Comparative study of catalyst effect on ethanol electrooxidation in alkaline medium: Pt- and Pd-based catalysts containing Sn and Ru, J. Electroanal. Chem. 9 (2020) 878.
[31] J. Guo, G. Sun, S. Shiguo, Y. Shiyou, Y. Weiqian, Q. Jing, Y. Yushan, X. Qin, Polyol-synthesized PtRu/C and PtRu black for direct methanol fuel cells, J. Power Sources 168 (2007) 299–306.
[32] J.L.G. de la Fuente, F.J. Pérez-Alonso, M.V. Martínez-Huerta, M.A. Peña, J.L.G. Fierro, S. Rojas, Identification of Ru phases in PtRu based electrocatalysts and relevance in the methanol electrooxidation reaction, Catal. Today 143 (2009) 69–75.
[33] H. Yan, S. Yao, B. Yin, W. Liang, X. Jin, X. Feng, Y. Liu, X. Chen, C. Yang, Synergistic effects of bimetallic PtRu/MCM-41 nanocatalysts for glycerol oxidation in base-free medium: structure and electronic coupling dependent activity, Appl. Catal. B Environ. 259 (2019) 118070. https://www.sciencedirect.com/science/article/pii/S0926337319308173.
[34] J.W. Da-Silva, A.J.G. Cobo, The role of the titania and silica supports in Ru-Fe catalysts to partial hydrogenation of benzene, Appl. Catal. Gen. 252 (2003) 9–16.
[35] Y.C. Wei, C.W. Liu, W.J. Chang, K.W. Wang, Promotion of Pt-Ru/C catalysts driven by heat treated induced surface segregation for methanol oxidation reaction, J. Alloys Compd. 509 (2011) 535–541.
[36] A.K. Choudhary, H. Pramanik, Enhancement of ethanol electrooxidation in half cell and single direct ethanol fuel cell (DEFC) using post-treated polyol synthesized Pt-Ru nano electrocatalysts supported on HNO_3-functionalized acetylene black carbon, Int. J. Hydrogen Energy 45 (2020) 574–594.
[37] F.J. Vidal-Iglesias, R.M. Arán-Ais, J. Solla-Gullón, E. Herrero, J.M. Feliu, Electrochemical characterization of shape-controlled Pt nanoparticles in different supporting electrolytes, ACS Catal. 2 (2012) 901–910.
[38] M. Watanabe, T. Mizukami, K. Tsurumi, T. Nakamura, P. Stoneharf, Activity and stability of ordered and disordered Co-Pt alloys for phosphoric acid fuel cells, J. Electrochem. Soc. 141 (1994) 2659–2668.
[39] S. Roy Chowdhury, S. Ghosh, S.K. Bhattachrya, Enhanced and synergistic catalysis of one-pot synthesized palladium-nickel alloy nanoparticles for anodic oxidation of methanol in alkali, Electrochim. Acta 250 (2017) 124–134.
[40] D.Y. Chung, K.J. Lee, Y.E. Sung, Methanol electro-oxidation on the Pt surface: revisiting the cyclic voltammetry interpretation, J. Phys. Chem. C 120 (2016) 9028–9035.
[41] M.A.F. Akhairi, S.K. Kamarudin, Catalysts in direct ethanol fuel cell (DEFC): an overview, Int. J. Hydrogen Energy 41 (2016) 4214–4228.
[42] D.P. Chen, X.C. Liu, X.D. Liu, L. Yuan, M.L. Zhong, C.Y. Wang, Pd nanoparticles on self-doping-defects mesoporous carbon supports for highly active ethanol oxidation and ethylene glycol oxidation, Int. J. Hydrogen Energy 46 (2021) 30455–30466.
[43] O. Guillén-Villafuerte, G. García, M.C. Arévalo, J.L. Rodríguez, E. Pastor, New insights on the electrochemical oxidation of ethanol on carbon-supported Pt

electrode by a novel electrochemical mass spectrometry configuration, Electrochem. Commun. 63 (2016) 48–51.
[44] J. Flórez-Montaño, G. García, O. Guillén-Villafuerte, J.L. Rodríguez, G.A. Planes, E. Pastor, Mechanism of ethanol electrooxidation on mesoporous Pt electrode in acidic medium studied by a novel electrochemical mass spectrometry set-up, Electrochim. Acta 209 (2016) 121–131.
[45] R. Rizo, A. Bergmann, J. Timoshenko, F. Scholten, C. Rettenmaier, H.S. Jeon, Y.T. Chen, A. Yoon, A. Bagger, J. Rossmeisl, B. Roldan Cuenya, Pt-Sn-Co nanocubes as highly active catalysts for ethanol electro-oxidation, J. Catal. 393 (2021) 247–258.
[46] J.C.M. Silva, S. Ntais, V. Rajaraman, É. Teixeira-Neto, Â.A. Teixeira-Neto, A.O. Neto, R.M. Antoniassi, E.V. Spinacé, E.A. Baranova, The catalytic activity of Pt:Ru nanoparticles for ethylene glycol and ethanol electrooxidation in a direct alcohol fuel cell, Electrocatalysis 10 (2019) 203–213.
[47] D.X. Yu, A.J. Wang, L.L. He, J. Yuan, L. Wu, J.R. Chen, J.J. Feng, Facile synthesis of uniform AuPd@Pd nanocrystals supported on three-dimensional porous N-doped reduced graphene oxide hydrogels as highly active catalyst for methanol oxidation reaction, Electrochim. Acta 213 (2016) 565–573.
[48] R. Kumar, E.T.S.G. da Silva, R.K. Singh, R. Savu, A.V. Alaferdov, L.C. Fonseca, L.C. Carossi, A. Singh, S. Khandka, K.K. Kar, O.L. Alves, L.T. Kubota, S.A. Moshkalev, Microwave-assisted synthesis of palladium nanoparticles intercalated nitrogen doped reduced graphene oxide and their electrocatalytic activity for direct-ethanol fuel cells, J. Colloid Interface Sci. 515 (2018) 160–171.
[49] S. Samad, K.S. Loh, W.Y. Wong, T.K. Lee, J. Sunarso, S.T. Chong, W.R. Wan Daud, Carbon and non-carbon support materials for platinum-based catalysts in fuel cells, Int. J. Hydrogen Energy 43 (2018) 7823–7854.
[50] A. Bach Delpeuch, M. Jacquot, M. Chatenet, C. Cremers, The influence of mass-transport conditions on the ethanol oxidation reaction (EOR) mechanism of Pt/C electrocatalysts, Phys. Chem. Chem. Phys. 18 (2016) 25169–25175.
[51] A.B. Calcerrada, A.R. de la Osa, J. Llanos, F. Dorado, A. de Lucas-Consuegra, Hydrogen from electrochemical reforming of ethanol assisted by sulfuric acid addition, Appl. Catal. B Environ. 231 (2018) 310–316.
[52] C. Lamy, T. Jaubert, S. Baranton, C. Coutanceau, Clean hydrogen generation through the electrocatalytic oxidation of ethanol in a Proton Exchange Membrane Electrolysis Cell (PEMEC): effect of the nature and structure of the catalytic anode, J. Power Sources 245 (2014) 927–936.
[53] E. Ruiz-López, E. Amores, A. Raquel de la Osa, F. Dorado, A. de Lucas-Consuegra, Electrochemical reforming of ethanol in a membrane-less reactor configuration, Chem. Eng. J. 379 (2020) 122289. https://www.sciencedirect.com/science/article/pii/S1385894719316833.
[54] A. Rodríguez-Gómez, F. Dorado, A. de Lucas-Consuegra, A.R. de la Osa, Additional pathways for the ethanol electro-reforming knowledge: the role of the initial concentration on the product yields, Fuel Process. Technol. 222 (2021) 106954. https://www.sciencedirect.com/science/article/pii/S0378382021002320.
[55] C. Xu, P.K. Shen, Electrochemical oxidation of ethanol on Pt-CeO2/C catalysts, J. Power Sources 142 (2005) 27–29.
[56] A.B. Calcerrada, A.R. de la Osa, H.A.E. Dole, F. Dorado, E.A. Baranova, A. de Lucas-Consuegra, Stability testing of PtxSn1 – x/C anodic catalyst for renewable hydrogen production via electrochemical reforming of ethanol, Electrocatalysis 9 (2018) 293–301.